

# Shape reconstruction and height fluctuations of red blood cells using defocusing microscopy

L Siman<sup>1</sup>, P M S Roma<sup>1</sup>, F T Amaral<sup>2</sup>, U Agero<sup>1</sup> and O N Mesquita<sup>1</sup>

<sup>1</sup>Departamento de Física, <sup>2</sup>Programa de Pós Graduação em Engenharia Elétrica, Universidade Federal de Minas Gerais, Caixa Postal 702, CEP 31270-901, Belo Horizonte, MG, Brazil

E-mail: mesquita@fisica.ufmg.br

October 2014

**Abstract.** In this paper the bright-field defocusing microscopy (DM) technique is presented. DM is able to obtain quantitative information of each plane/surface of pure phase objects, as live unlabeled cells, and its application to red blood cells (RBCs) is demonstrated. Based on contrast, simple methods to obtain thickness profile and three dimensional (3D) total reconstruction of RBCs are proposed and the actual height profiles of upper and lower surface-membranes (lipid bilayer/cytoskeleton) of discocyte and stomatocyte red cells are presented as examples. In addition, using the mean square contrast fluctuation and modeling the RBC membranes fluctuations spectra as dependent of a bending modulus ( $\kappa_c$ ), a surface tension ( $\sigma$ ) and a confining potential ( $\gamma$ ) term, slowly varying quantities along the cell radius, a genetic algorithm (GA) is used and the radial height fluctuations of each surface-membrane are accessed, separately. The radial behaviors of  $\kappa_c$ ,  $\sigma$  and  $\gamma$  are also obtained, allowing the discussion of physical aspects of the RBC membrane.

## 1. Introduction

The links between cells mechanics and human diseases have been subject of considerable scientific research effort for a number of decades. For example, pathological conditions affecting red blood cells (RBCs) can lead to alterations to the cell's shape [1]. Also, changes in RBC membrane properties have influence in the cell deformability and alters blood circulation [1]. In that sense, there is an increasing interest in the development of new techniques able to study mechanical properties of cells.

Optical microscopy has been shown to be a valuable tool to study biomechanics of living cells, since it can be performed with minimal perturbation in the cells. The aim of this work is to present new methods to measure optical and mechanical characteristics of RBCs using defocusing microscopy (DM)[2, 3, 4, 5, 6, 7, 8, 9], a simple, yet powerful optical microscopy technique capable to access information of each surface-membrane (lipid bilayer/cytoskeleton) of living cells. We will show, in the case of an adhered red

cell, that information along the  $x, y$  position of the upper surface-membrane, free to fluctuate, can be separately obtained from information along the  $x, y$  position of the lower surface-membrane, which is adhered to the substrate.

Since the contrast of cells without the addition of exogenous contrast agents is very weakly viewed through a standard bright-field microscope, the traditional optical microscopy techniques used to observe living cells are phase-contrast and Nomarski [10, 11]. These techniques provide qualitative information or require major calibration to provide the object's phase map. A number of other optical microscopy techniques capable to obtain full-field quantitative phase information have been recently developed [12, 13, 14, 15]. A recent review about these techniques applied to red blood cells can be found in [16]. As an example, shape and membrane fluctuations of red blood cells have been measured using diffraction phase microscopy (QPM) [15, 17, 18], an interferometric imaging technique that provides quantitative maps of the optical paths across living cells. DM is a bright-field microscopy technique also based on interferometric imaging, but with the advantage of having a simpler experimental set up than QPM, besides being able to obtain shape and membrane fluctuations of each surface-membrane of living cells, separately.

Transparent objects that would be invisible in a standard bright-field optical microscope can turn visible by defocusing the microscope, which occurs because the act of defocusing introduces a phase difference between the diffracted and non-diffracted orders. By recording images at two different focal positions, one can get information about the phase of the optical electric field and obtain the objects full-field phase map. The formalism of Transport Intensity Equation [19] has been used for this aim [12, 13, 14], but in its present form there are no explicit phase terms considering the distance between the focal plane and the diffracting surfaces, in a way that the complete characterization of all interfaces of a phase object is not feasible. A defocusing technique has been recently applied for 3D imaging of cells using a phase contrast microscope under white light illumination, with transverse resolution of 350 nm and axial resolution of 900 nm [20]. This technique cannot resolve surfaces separated by an axial distance smaller than 900 nm, which is the case of most RBCs. Strikingly, the defocusing microscopy technique presented here can resolve surface-membranes of RBCs separated by axial distances down to 300 nm, such that cells subject to isotonic, hypertonic and hypotonic solutions can be fully reconstructed [7].

To determine the DM contrast caused by a red cell, a light electric field is propagated through an infinity corrected defocused microscope model using the Angular Spectrum propagation formalism [21]. Our approach is limited by the paraxial approximation, such that the problem is treated within Fresnel diffraction theory and neglects light polarization. Using the contrast, simple methodologies to retrieve refractive index, surface area, volume and three dimension (3D) thickness reconstruction of red cells are proposed. Also, with the use of a simple computational method the height profiles of the cell upper and lower surface-membranes are separately determined [7]. Here a new application in RBC is presented, showing the method's potential for studying the

deformation in red cells shape caused by diseases. Due its simplicity and accessibility, the developed method can be adopted by non-specialists.

An important measurement when studying cell membranes is the RMS displacement of the membrane height fluctuations  $u_{rms} = \sqrt{u^2}$ , where  $u$  is the cell normal displacement around the equilibrium position  $h$ . In red cells this phenomena is known as RBC flickering and was first quantified in 1975 by Brochard and Lenon [22]. More recent models use the well established fact that the RBC surface is composed of an outer lipid bilayer and an inner cytoskeleton, a quasi-two-dimensional network of spectrin proteins [23] sparsely connected to the lipid membrane through specialized proteins, such that this coupled membrane is characterized by effective elastic moduli: bending modulus  $k_c$ , tension  $\sigma$  and confining potential  $\gamma$ , resulting in a fluctuation spectrum in the planar approximation given by,

$$\langle |u(\vec{q})|^2 \rangle = \frac{k_B T}{\kappa_c q^4 + \sigma q^2 + \gamma}, \quad (1)$$

where  $q$  is the fluctuation wavenumber,  $T$  is the absolute temperature and  $k_B$  is the Boltzmann constant. If non-thermal noise due to detachment of the cytoskeleton from the lipid bilayer caused by ATP interaction is considered,  $T$  is replaced by an effective temperature, which is higher than the bath temperature [17, 23, 24]. The fluctuation spectrum of equation 1 has been used for analysis of the flickering phenomena of RBCs [6, 25]. In [6] we have used it to fit the DM mean square contrast fluctuation data measured only in at the center of the cell, showing the technique's ability to access membrane fluctuations,  $k_c$  and  $\gamma$  of each surface-membrane of RBCs. Here we also assume this spectrum and with the use of a genetic algorithm (GA), the height fluctuations  $u_{rms}$  along the radius of each red cell surface-membrane are extracted from DM fluctuation contrast data. The radial behaviors of the elastic moduli are also extracted, allowing the discussion of mechanical aspects of RBC surface-membranes. Although the choice of a fluctuation spectrum is a requisite, the ability to obtain  $u_{rms}$  do not dependent on the chosen model. By using the planar membrane model of equation 1 a more direct comparison with results obtained by other techniques can be carried out. As an example, the area compressibility moduli  $KA$  obtained here from our  $\gamma$  results are in agreement with the values measured for whole RBCs using DPM technique [18]. Finally, in order to test the validity and accuracy of DM technique, a set of control experiments using phase gratings were performed and are presented in the Supplemental material. The grating's height profiles and refractive indexes were measured using well establish methods and compared with the results obtained using DM technique.

### 1.1. Defocusing microscopy

A bright-field microscope with infinity corrected optics is illustrated in figure 1(A). Light emitted from a halogen lamp passes through the microscope condenser system aligned in Köhler configuration [21], such that plane waves with uniform intensity (colour filtered leaving only the appropriate frequency transmitted) lighten the object. After passing

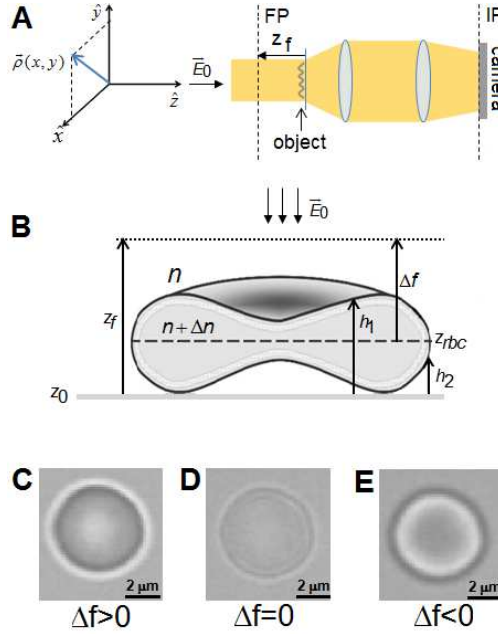


**Figure 1.** (A) Scheme of a bright-field microscope with infinity corrected optics. If the optical axis is defined as the  $z$  axis, with its origin at the coverslip position, the defocus distance  $z_f$  is given by the distance between the object and the objective focal plane (FP). (B) Model for a RBC observed through a defocused microscope. The cell has a refractive index of  $n + \Delta n$ , where  $n$  is the immersion medium refractive index and  $h_1$  and  $h_2$  are the distances between the coverslip and upper and lower membrane, respectively. The distance  $\Delta f$  between the cell mean plane ( $z_{rbc}$ ) and the objective focal plane is used during the experiments to quantify the defocus amount. Three contrast images of a cell in: (C)  $\Delta f > 0$ , (D)  $\Delta f = 0$  and (E)  $\Delta f < 0$ .

through the specimen both transmitted and diffracted rays are collected by the objective lens, which together with the tube lens create an amplified image of the object at the image plane (IP). Assuming the reference system in figure 1(A), where  $z$  is the optical axis, the origin can be set anywhere along it. The origin is set at the coverslip plane and the defocus distance ( $z_f$ ) is defined as the distance between the coverslip and the objective focal plane (FP). If the observed specimen is a thin pure phase object placed at FP, no contrast can be seen at IP. When the object is slightly shifted from FP a contrast  $C$  is observed. This contrast is named here as DM contrast and defined as  $C(\vec{\rho}) = \frac{I(\vec{\rho}) - I_0}{I_0}$ , where  $I(\vec{\rho})$  is the light intensity at a point  $\vec{\rho}$  of the image plane and  $I_0$  is the background intensity of the same plane. It is important to mention that DM technique does not require the use of an infinity corrected optical system, but it is fundamental to have a homogenous illumination.

Red cells can be treated as pure phase objects when illuminated by red light because in this case light absorption is negligible. Therefore the incident light is filtered, letting a transmitted light with  $\lambda = (0.660 \pm 0.010) \mu\text{m}$ . As shown in figure 1(B), RBCs can be modeled as objects composed of an upper and a lower surface-membrane (lipid bilayer + cytoskeleton), separated by a typical distance of  $2 \mu\text{m}$  at the rim. Taking the coverslip

plane as the  $z$  axis origin,  $h_1$  is defined as the distance between the coverslip and the cell upper membrane,  $h_2$  as the distance between the coverslip and the lower membrane and  $H = h_1 - h_2$  as the cell thickness. The cell is considered to have an uniform refractive index  $n_{rbc} = n + \Delta n$ , where  $n$  is the immersion medium refractive index. Performing the propagation for an electric field  $E_0$  with wave number  $\vec{k} = k_0 \hat{z}$  (Supplementary material), for first order diffraction, the contrast  $C(\vec{\rho})$  is given by,

$$C(\vec{\rho}) = \frac{2\Delta n k_0}{\sqrt{S}} \left\{ \sum_{\vec{q}} \left[ h_2(\vec{q}) \sin\left(\frac{(z_f - h_2(\vec{\rho}))q^2}{2k}\right) - h_1(\vec{q}) \sin\left(\frac{(z_f - h_1(\vec{\rho}))q^2}{2k}\right) \right] \sin(\vec{q} \cdot \vec{\rho}) \right\}. \quad (2)$$

Here  $k_0$  is the vacuum illumination light wavenumber,  $\Delta n$  is the refractive index difference between the immersion medium and the RBC,  $S$  is the cell surface area and  $k = n_{ob}k_0$ , where  $n_{ob}$  is the objective immersion medium refractive index. The terms  $h_{1/2}(\vec{q})$  are the spatial Fourier components of the phase object height profiles  $h_{1/2}(\vec{\rho}) = \frac{1}{\sqrt{S}} \sum_{\vec{q}} h_{1/2}(\vec{q}) \sin(\vec{q} \cdot \vec{\rho})$ . Considering  $\frac{(z_f - h_1)q^2}{2n_{ob}k_0} \ll 1$ ,  $\frac{(z_f - h_2)q^2}{2n_{ob}k_0} \ll 1$ , and  $\frac{1}{\sqrt{S}} \sum_{\vec{q}} \left( h(\vec{q}) \sin(\vec{q} \cdot \vec{\rho}) q^2 \right) = -\nabla^2 h(\vec{\rho})$ , we obtain the DM contrast for a RBC,

$$C(\vec{\rho}) \simeq \frac{\Delta n}{n_{ob}} \left[ \left( z_f - h_1(\vec{\rho}) \right) \nabla^2 h_1(\vec{\rho}) - \left( z_f - h_2(\vec{\rho}) \right) \nabla^2 h_2(\vec{\rho}) \right]. \quad (3)$$

The validity of equation 3 can be determined for the interval that  $C$  varies linearly with  $z_f$ . This approximation will be used for 3D total reconstruction of RBCs since the average shape involves low wavenumbers  $q$ . For fluctuation analysis, the complete equation 2 has to be used, as shown below. In DM formulation there is no doubt over which wavenumber of light to be used, since the phase shift introduced by each optical element causing the image defocusing is known. If defocusing is generated by displacing an oil immersion objective, the phase shift introduced is related to optical path difference in that medium and the wavenumber to be used in the defocusing term is  $k = k_0 n_{ob} = k_0 \times 1.51$ . Differently, if defocusing is generated by displacing a dry objective, then  $k = k_0 n_0 = k_0$ .

An important characteristic of cell membranes is their height fluctuation in relation to their average position. Those height fluctuations induce contrast fluctuations and the mean square contrast fluctuation ( $\langle (\Delta C)^2 \rangle$ ) contains information about them, such that the elastics moduli can be extracted. In this case, each height profile is described by a constant term  $h_{1/2}$  and a time-dependent fluctuating term  $u_{1/2}$ , so that  $h_{1/2}(\vec{\rho}, t) = h_{1/2}(\vec{\rho}) + u_{1/2}(\vec{\rho}, t)$ . The contrast fluctuation  $\Delta C(\vec{\rho}, t) = C(\vec{\rho}, t) - \langle C(\vec{\rho}, t) \rangle$ , where  $\langle C(\vec{\rho}, t) \rangle$  is the mean contrast over time gives,

$$\begin{aligned} \langle \Delta C^2(\vec{\rho}) \rangle = & \frac{(2\Delta n k_0)^2}{2S} \sum_{\vec{q}} \left[ \langle |u_1(\vec{q})|^2 \rangle \times \sin^2\left(\frac{z_f - h_1(\vec{\rho})}{2k} q^2\right) \right. \\ & \left. + \langle |u_2(\vec{q})|^2 \rangle \sin^2\left(\frac{z_f - h_2(\vec{\rho})}{2k} q^2\right) \right], \end{aligned} \quad (4)$$

where  $\langle |u_{1/2}^2(\vec{q})|^2 \rangle$  are the membranes fluctuation spectra. Equation 4 has two minima: when  $z_f = h_1(\vec{\rho})$  and when  $z_f = h_2(\vec{\rho})$ . By scanning  $z_f$  and measuring  $\langle (\Delta C)^2 \rangle$  at the center of RBCs, Glionna et al. [6] showed that these two minima for  $\langle (\Delta C)^2 \rangle$  are displayed and it was possible to determine the elastics constants at the center of the cell, for each membrane, separately.

## 2. Materials and methods

### 2.1. Microscopy

All experiments were conducted on inverted microscopes operating in bright-field (Nikon TE300 and Nikon Eclipse Ti, Nikon Instruments Inc., Melville, NY) with a 100X oil immersion objective (Nikon Plan APO DIC H, 1.3 NA, Nikon). Images were either captured with a CMOS camera of  $640 \times 480$  pixels, (Silicon Video SV642M, EPIX Inc, Buffalo Grove, IL) at a typical frame rate of 333fps, or with a CCD camera of  $1390 \times 1037$  pixels (UP1800CL-12B, UNIQ Vision Inc, Santa Clara, CA) at 15fps, depending on the experiment. The defocusing distance was controlled by a piezoelectric nanoposition stage (P563-3CD, Physik Instrumente (PI) GmbH Co, Karlsruhe) with precision of 5 nm or by using the Nikon Perfect Focus System. The cells were illuminated with red filtered light ( $\lambda = (0.660 \pm 0.010) \mu\text{m}$ ).

### 2.2. Sample preparation

Red blood cell samples were prepared by a standard procedure to yield discocyte RBCs [5], with informed consent from the human subjects. For each experiment 500  $\mu\text{L}$  of RBC suspension was transferred into a microscope coverslip chamber and covered to avoid water evaporation. All experiments were performed at room temperature ( $T = 299 \text{ K}$ ).

### 2.3. Cell imaging

For RBCs experiments it is convenient to settle the  $z$  axis origin at the cell mean plane ( $z_{rbc}$ ), so that  $z_f = \Delta f + z_{rbc}$ , where  $\Delta f$  is the distance between the cell mean plane and the objective focal plane (figure 1 (B)). Also,  $h_1$  and  $h_2$  are defined as the distances between  $z_{rbc}$  and the upper and lower membrane, respectively, and the cell thickness is now given by  $H = h_1 + |h_2|$ . The mean plane is easily determined during cell imaging as the minimal contrast plane along the  $z$  axis. In figure 1(C,D,E), RBC images for  $\Delta f > 0$ ,  $\Delta f = 0$  and  $\Delta f < 0$  are presented. For shape results, 42 RBCs were imaged for 20 seconds at defocus positions  $\Delta f = 2 \mu\text{m}$  ( $C_1$ ) and  $\Delta f = 0$  ( $C_2$ ), at a frame rate of 15 fps with the UNIQ camera. For membrane fluctuations results the same 42 cells were imaged for 30 seconds at defocus position  $\Delta f = 2 \mu\text{m}$  and using a frame rate of 333 fps with the CMOS camera. It is important to mention that several cells can be imaged simultaneously, regarding that they are not in contact with each other. Using plugins developed by our group,  $\langle C(\vec{\rho}) \rangle$  and  $\langle (\Delta C(\vec{\rho}))^2 \rangle$ , where the averages are

time averages, were obtained for each stack of images. The camera noise was subtracted from all  $\langle (\Delta C(\vec{\rho}))^2 \rangle$  data.

### 3. Results and discussion

#### 3.1. Thickness profile

To obtain RBC thickness reconstruction and volume we use equation 3 and subtract the cell average contrast taken at two different defocus distances,  $\langle C_1(\vec{\rho}) \rangle$  and  $\langle C_2(\vec{\rho}) \rangle$ . Performing a Fourier transform (FFT) on it, the laplacian term becomes  $-q^2(h_1 - h_2)$ , where  $H(\vec{\rho}) = h_1 - h_2$  is the cell thickness. Dividing it by  $(-q^2)$  and performing an inverse Fourier Transform,

$$H(\vec{\rho}) = \frac{n_{ob}}{\Delta n(z_{f_2} - z_{f_1})} \mathcal{F}^{-1} \left\{ \frac{\mathcal{F}\{\langle C_1(\vec{\rho}) \rangle - \langle C_2(\vec{\rho}) \rangle\}}{-q^2} \right\}, \quad (5)$$

the cell thickness is then obtained. The spatial average intensity of the entire image  $\langle I \rangle_{\vec{\rho}} = \frac{1}{A_0} \int I d\vec{\rho}$  of a pure phase object is a constant, given by the background intensity  $\langle I \rangle_{\vec{\rho}} = I_0$ . That implies that the average contrast  $\langle \langle C \rangle \rangle_{\vec{\rho}} = (\langle I \rangle - I_0)/I_0 = 0$  for the entire image. Since the Fourier transform of the contrast for  $q = 0$  is  $\langle C \rangle = 0$ , we disregard this point in equation 5, eliminating the problem of the division by  $q = 0$ . This algorithm (equation 5) was previously proposed in [12] to retrieve the phase map of pure phase objects. However, since the phase was not explicitly solved, the object's thickness profile was not obtained. The above procedure can be easily performed using Image J (Rasband WS. ImageJ, U.S. National Institutes of Health, Bethesda, Maryland, USA, [imagej.nih.gov/ij/](http://imagej.nih.gov/ij/), 19972012) [26]. Since the values for  $z_f$ ,  $n_{ob}$  and  $\Delta n$  are known, the resultant image is a thickness map of the observed cell, which corresponds to the cell's phase map when divided by  $\Delta n$ . The cell refractive index can also be determined using DM measurements and the procedure is exposed in [7]. Here the value of  $\Delta n = 0.058 \pm 0.003$  is used. Cell volume can be determined as  $V = A_{pixel} \times H$ , using the pixel area  $A_{pixel}$ . A 3D thickness image can be visualized using the 3D Surface Plot plug in from Image J [26]. In figure 2(A), a red cell thickness map is shown together with its 3D thickness reconstruction. On the right side, the thickness profile plot along a horizontal line of the thickness map is presented. The mean volume for the 42 analyzed cells was  $\bar{V} = 93 \pm 19 \mu\text{m}^3$ , which is within the range reported by other techniques [27].

#### 3.2. 3D total imaging

An unique capability of DM is to image the upper and lower surfaces of a phase object, what we call 3D total imaging. To determine the height profiles of the cell upper and lower surface-membranes, separately, the cell thickness profile and the contrast image for one single defocus position,  $C_1(\vec{\rho})$ , is used. Defining the asymmetry between the

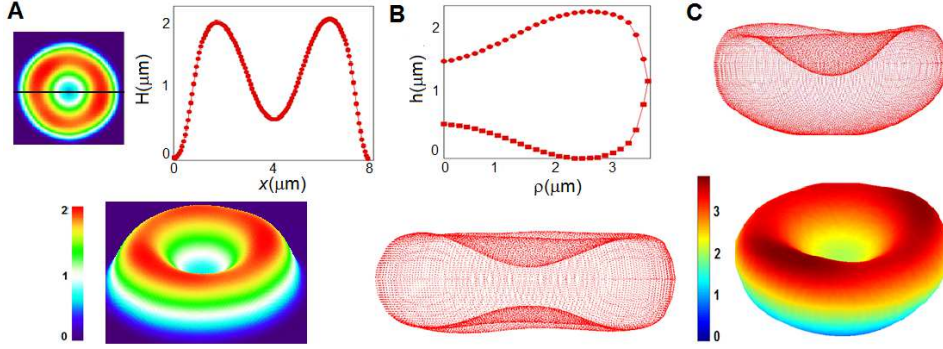


**Figure 2.** (A) Thickness map of a red cell and its 3D thickness reconstruction. The plot shows the cell thickness  $H$  along the horizontal line drawn in the thickness map. (B) Radial height profiles for upper (points) and lower (squares) membranes of a RBC and its 3D total image. (C) 3D total image of a stomatocyte RBC in two different views and representation. Color bars in  $\mu\text{m}$ .

cell's membranes as  $\delta(\vec{\rho}) = h_1 - |h_2|$ , for  $z_f = 0$ , equation (3) can be rewritten as,

$$\nabla^2 \delta + \frac{\nabla^2 H}{H} \delta = -\frac{2n_{ob}}{H \Delta n} C(0, \vec{\rho}). \quad (6)$$

Equation 6 is a non-homogeneous Helmholtz equation with variable coefficients that is numerically solved for  $\delta(\vec{\rho})$  with the initial condition  $\delta(\vec{\rho}) = 0$  [7]. From the returned asymmetry  $\delta(\vec{\rho})$ , the surface-membranes height profiles for each pixel of the contrast image are recovered,

$$h_1(\vec{\rho}) = \frac{H(\vec{\rho}) + \delta(\vec{\rho})}{2} \quad h_2(\vec{\rho}) = \frac{-H(\vec{\rho}) + \delta(\vec{\rho})}{2} \quad (7)$$

and the total 3D imaging is obtained. Using the developed method the height profiles  $h_1$  and  $h_2$  for the 42 analyzed cells were performed. In figure 2(B) an example of the radial height profiles  $h_1$  (red points) and  $h_2$  (red squares) for a RBC, together with its 3D total image is presented. In figure 2(C) different representations of two views of the 3D total image of a stomatocyte red cell are also presented. As one can see, the 3D total imaging method access the actual bowl-like shape of the stomatocyte cell, showing that DM technique could be useful to investigate the relation between red cells deformation and pathologies, as well as adhesion to substrates. Further details of the method can be seen in [7].

*3.2.1. DM axial resolution* DM axial resolution is based on the sensitivity of image contrast measurement, optical contrast of the phase object and mean curvature of the surfaces visualized. For an estimate, let us determine the difference in contrast (equation 3) between the two surfaces at  $\vec{\rho} = 0$ , where the minimum distance between the membrane-surfaces occurs in normal RBCs,

$$\Delta C = \frac{\Delta n}{n_{ob}} (h_1 - h_2) (\nabla^2 h_1 - \nabla^2 h_2) = \frac{\Delta n}{n_{ob}} H(0) \nabla^2 H(0). \quad (8)$$



Here  $H(0) = h_1(0) - h_2(0)$  is the axial distance between the two surface-membranes in the center of the cell. The minimum axial distance that can be resolved using DM is then,

$$H(0)_{min} = \frac{n_{ob}\Delta C_{min}}{\Delta n \nabla^2 H(0)}. \quad (9)$$

Considering a contrast sensitivity of  $\Delta C_{min} = 10^{-2}$ , the oil immersion refractive index  $n_{ob} = 1.51$  and the typical values for isotonic RBCs,  $\Delta n = 0.058$ , and  $\nabla^2 H(0) = 1.7 \mu\text{m}^{-1} = 1.7 \times 10^{-3} \text{ nm}^{-1}$ , then  $H_{min}(0) \sim 150 \text{ nm}$ , allowing clear visualization of the two RBC surfaces.

### 3.3. Surface-membranes height fluctuation

In order to access RBC surface fluctuations one can measure the mean square contrast fluctuation  $\langle (\Delta C)^2 \rangle$  at one defocus distance. Using the continuum version of equation 4,

$$\begin{aligned} \langle \Delta C^2(\vec{\rho}) \rangle = & \frac{(\Delta n k_0)^2}{\pi} \int_{q_{min}}^{q_{max}} q dq \left[ \langle |u_1(q)|^2 \rangle \times \sin^2 \left( \frac{(z_f - h_1)q^2}{2k} \right) + \right. \\ & \left. \langle |u_2(q)|^2 \rangle \times \sin^2 \left( \frac{(z_f - h_2)q^2}{2k} \right) \right], \end{aligned} \quad (10)$$

and the profiles for  $h_1(\vec{\rho})$  and  $h_2(\vec{\rho})$  we previously obtained, then the fluctuation power spectra  $|u_{1/2}(\vec{q})|^2$  as in equation 1 and the RMS height fluctuation of each cell membrane can be determined by computational methods. A genetic algorithm was implemented and employed (Supplementary material) and the results for  $u_{1/2(rms)}$ ,  $k_{c1/2}$ ,  $\gamma_{1/2}$  and  $\sigma_{1/2}$  for an average of 42 RBCs are presented. For the GA fittings the continuum form of equation 4 is used. The integration approach is appropriate to the red cell membrane deformation and the results are not very sensitive to the exact values of the limits  $q_{min}$  and  $q_{max}$ . Assuming the elastic constants as slowly varying functions of  $\vec{\rho}$ , an adiabatic approximation can be done by assuming a piecewise constant spectrum. The integration intervals used are  $q = [0.6, 12.0] \mu\text{m}^{-1}$  for the upper membrane and  $q = [1.2, 12.0] \mu\text{m}^{-1}$  for the lower one. The minimum value of  $q$  corresponds to the first zero of the Bessel function for the cell radius  $R = 4 \mu\text{m}$  (upper membrane) and for a radius of  $R = 2 \mu\text{m}$  (lower membrane). This difference occurs because the lower membrane is attached to the substrate for  $R > 2 \mu\text{m}$  (figure 2(B)), reducing some possible wavenumbers. The maximum value for  $q$  is determined by the objective numerical aperture,  $q \sim 12 \text{ rad}/\mu\text{m}$ .

In figure 3 (A) the average for 42 cells of the mean square contrast fluctuation  $\langle (\Delta C)^2 \rangle$  at  $\Delta f = 2 \mu\text{m}$ , after camera noise subtraction, is displayed. The blue area represents the ten final fittings returned by the AG and the small deviation indicates that the chosen plane membrane model yields a good fitting of the experimental data. On the plot inset, the temporal contrast autocorrelation function along a line in the cell center (black dots) and along a line in the image background (green dots) are shown. As it can be seen, for the sampling time used the background time correlation function consists of a term in  $t = 0$  (shot-noise) and decays immediately to zero. This shot noise

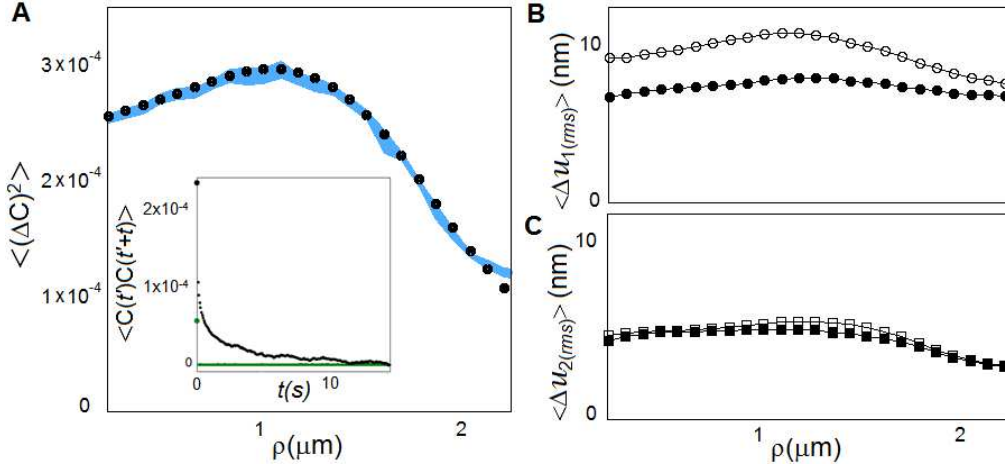


**Figure 3.** (A) Average of the mean square contrast fluctuation  $\langle (\Delta C)^2 \rangle$  at  $\Delta f = 2 \mu\text{m}$  (dots) for 42 RBCs. The blue area represents the ten final fittings returned by the AG. Inset: time autocorrelation function of contrast on the RBC and on the background, which presents only a shot-noise at  $t = 0$ . (B) RMS height fluctuation of the upper membrane  $u_{1(rms)}$  before (empty dots) and after (full dots) correction for cell lateral movement. (c) RMS height fluctuation of the upper membrane  $u_{2(rms)}$  before (empty squares) and after (full squares) correction.

is subtracted from the contrast fluctuations data measured in the cells. We observe that a good signal to noise ratio is obtained down to  $\langle (\Delta C)^2 \rangle \sim 2 \times 10^{-6}$ , returning a sensitivity of about 1.4 nm in the measurements of height fluctuations.

The RMS displacement of membrane height fluctuations  $u_{1(rms)}$  and  $u_{2(rms)}$  are shown in figure 3(B-C). Four sets of data are presented and the ones depicted by empty dots and squares represent the upper and lower membrane  $u_{rms}$ , respectively. The membranes have a similar height fluctuation profile, but the upper membrane fluctuates more than the lower one, since the lower membrane is closer to the substrate and adhered to it in a certain region, confining and restricting membrane fluctuations. The two other curves (full dots and squares) in the graph represent  $u_{1(rms)}$  and  $u_{2(rms)}$  after being corrected for the cell lateral movement. The correction term is  $\sqrt{4 - 3 \cos^2(\theta)}$  and it is fully deduced in the Supplementary material. In [27], *Rappaz et al.* suggested a different correction, where the height fluctuation amplitudes are modified by a factor  $\cos(\theta)$ , with  $\theta$  the angle that the normal to the cell surface makes with the  $z$  axis. Since DM technique can access the height profile of each cell membrane, our proposed correction might be more accurate.

### 3.4. Confining potential $\gamma$

The confining potential  $\gamma$  of the fluctuation spectrum of equation 1 is a term that prevents a planar surface to move away from its equilibrium position (for  $q = 0$  mode). For a planar membrane close to a substrate, if the membrane/substrate interaction can be modeled by a harmonic potential, then the confining potential is a measure of its

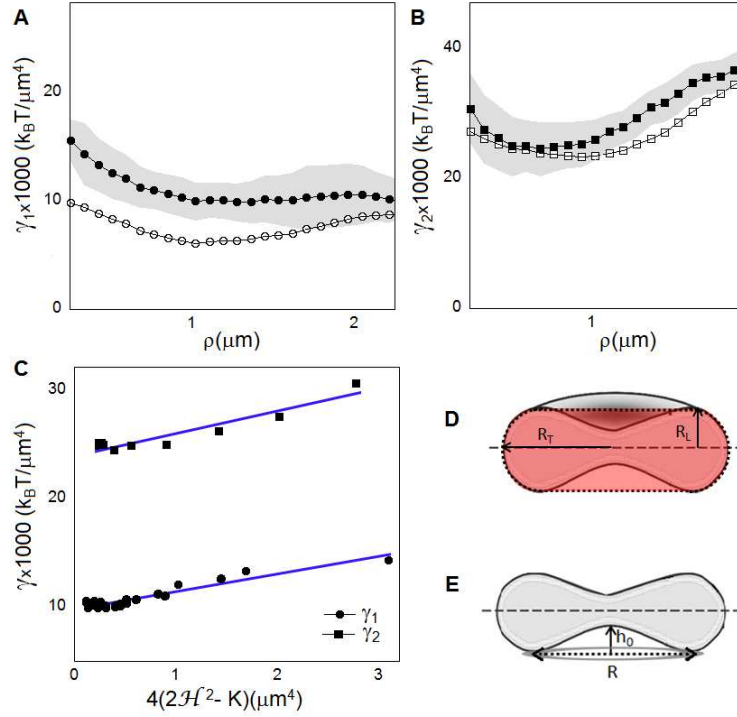


**Figure 4.** Confining potential for each cell membrane: (A)  $\gamma_1$  and (B)  $\gamma_2$ . The unfilled symbols represent the non-corrected data and the filled symbols represent the corrected ones. The grey area is the standard deviation of the mean value obtained with the ten final runs of the AG. (C)  $\gamma$  versus  $4(2\mathcal{H}^2 - K)$  for each membrane with the linear fit  $\gamma = KA \times 4(2\mathcal{H}^2 - K) + \gamma_0$ . The returned values for the compressibility moduli are  $KA_1 = (1.6 \pm 0.1) \times 10^3 k_B T / \mu m^2 \sim 7 \mu N/m$  and  $KA_2 = (2.0 \pm 0.3) \times 10^3 k_B T / \mu m^2 \sim 8 \mu N/m$ . Also,  $\gamma_{01} = (9.9 \pm 0.1) \times 10^3 k_B T / \mu m^4$  and  $\gamma_{02} = (24.0 \pm 0.4) \times 10^3 k_B T / \mu m^4$ . (D) Representation of the cylindrical-torus shell proposed, with principal curvatures  $C_L = \frac{1}{R_L}$  and  $C_T = \frac{1}{R_T}$ . (E) Illustration of a RBC membrane area delimited by a circumference of radius  $R \sim 2 \mu m$ .

spring constant per unit area [29]. In the RBC composite membrane model proposed by *Auth et al.* [23], the connection of the spectrin-cytoskeleton to the lipid bilayer is modeled by a confining potential, such that the lipid bilayer remains sparsely attached to the cytoskeleton by entropic springs and kept at an average distance from it. Differently, in closed-shell membrane models the shell size is limited by the membrane total finite size and the confining potential is associated to the restoring force due to an area expansion/compression resultant of the shell breathing mode ( $q = 0$ ) [18]. In figure 4(A) and (B) our measurements for  $\gamma_1$  and  $\gamma_2$  are presented, respectively. The values are within the range of  $[5 - 50] \times 10^3 k_B T / \mu m^4 = [20 - 200] \times 10^6 J/m^4$  (assuming  $T$  as the bath temperature). The empty symbols represent the data before correction for lateral movement and the full ones represent the data after correction. The grey area is the standard deviation of the mean value obtained with the ten final runs of the AG.

By analyzing the data we propose that two types of confining potential are at work: one related to the cell local curvature and another related to the cell overall shell

shape, named here as local and global potentials, respectively. In the RBC spherical shell model proposed by *Park et al.*[18] the cell is treated as a spherical shell and the confining potential is associated to the restoring force that appears due to spatially uniform radius displacements ( $q = 0$  breathing mode). For this deformation, the simple surface energy [30],

$$f_t = \frac{KA}{2} \left( \frac{\Delta A}{A} \right)^2 \quad (11)$$

can be considered, where  $KA$  is the area compressibility modulus,  $A$  is the surface area ( $A = 4\pi R^2$ , for a spherical shell of radius  $R$ ) and  $\Delta A$  is the area increase/decrease. If the shell has an equilibrium radius  $R_0$ , a radial displacement  $u$  costs an energy,

$$f_t = 2KA \frac{u^2}{R_0^2} = 2KA \frac{2}{R_0^2} \frac{u^2}{2} = \gamma \frac{u^2}{2}, \quad (12)$$

neglecting  $u^4$  terms. For general surface shapes, with principal curvatures  $C_1$  and  $C_2$ ,

$$f_t = 2KA \left( C_1^2 + C_2^2 \right) \frac{u^2}{2} = 4KA(2\mathcal{H}^2 - K) \frac{u^2}{2}, \quad (13)$$

which defines,  $\gamma = 4KA(2\mathcal{H}^2 - K)$ , where  $\mathcal{H}$  is the surface mean curvature and  $K$  is the Gaussian curvature. In figure 4(C) the plots of  $\gamma$  versus  $4(2\mathcal{H}^2 - K)$  for each membrane are presented. The linear equation  $\gamma_{1/2} = KA_{1/2} \times 4(2\mathcal{H}_{1/2}^2 - K_{1/2}) + \gamma_{0_{1/2}}$  fits reasonably well both data and returns similar values for the compressibility modulus  $KA_1 = (1.6 \pm 0.1) \times 10^3 k_B T / \mu m^2 \sim 7 \mu N/m$  and  $KA_2 = (2.0 \pm 0.3) \times 10^3 k_B T / \mu m^2 \sim 8 \mu N/m$  (assuming  $T$  as the bath temperature). Those values are of the order of half the ones reported by *Park et al.* in [18], where they found a value of  $\sim 18 \mu N/m$  for whole discocyte RBCs. From the linear fit it becomes clear the existence of a potential term  $\gamma_0$ , which is proposed here to be a global potential responsible to keep the overall shape of the cell. The values of  $\gamma_0$  found for the upper and lower membranes are  $\gamma_{0_1} \sim 10 \times 10^3 k_B T / \mu m^4$  and  $\gamma_{0_2} \sim 24 \times 10^3 k_B T / \mu m^4$ , respectively. It is important to mention that for the upper membrane fitting all RBC region for  $\gamma_1$  was used, while only the more central region ( $\rho \leq 1 \mu m$ ) of the cell, far from the adhesion region, was used for  $\gamma_2$ .

To model the global potential  $\gamma_{0_1}$  for the upper membrane a more realistic description of the red cell shape is used. The cell is treated as a cylindrical-torus shell (figure 4(D)), such that its two curvatures are  $(1/R_T)$  and  $(1/R_L)$ , with a potential (equation 13),

$$\gamma_{0_1} = 2KA_1 \left( \frac{1}{R_L^2} + \frac{1}{R_T^2} \right). \quad (14)$$

Considering  $R_T$  as the RBC radius measured experimentally  $R_{rbc} \sim 4 \mu m$ , such that  $1/R_T \sim 0.25 \mu m^{-1}$ , and using the value for  $KA_1$  previously measured, one obtains that  $\gamma_{0_1} \sim 10 \times 10^3 k_B T / \mu m^4$  coincides with equation 14 if  $R_L \simeq 0.6 \mu m$ . From figure 4(D), a good approximation for the lateral radius  $R_L$  is given by half of the cell maximum thickness  $H_{max}/2 \sim 1 \mu m$ . Finally, it is noteworthy to mention that the main contribution to  $\gamma_1$  comes from the cylindrical-torus term and not from the local curvature

term  $2\mathcal{H}^2 - K$  of the upper membrane, indicating that the restriction to fluctuation is mostly due the cylindrical envelope, rather than due the sparse connections between the cytoskeleton and the lipid bilayer, as proposed by *Gov et al.* [31].

In order to model the global confining potential  $\gamma_{0_2}$  the lower membrane is treated as a spherical cap of radius  $R_0$  and height  $h_0$  able to deform in height but not in radius. This assumption takes into account that the lower membrane is attached to the substrate and thus fixed in a circumference of radius  $R$ , as depicted in figure 4(E). For the cap surface area  $A_0 = 2\pi R_0 h_0$ , a deformation  $u$  in the cap's height costs an energy (equation 11),

$$f_t = \frac{KA}{2} \left( \frac{\Delta A}{A} \right)^2 = \frac{KA}{2} \frac{u^2}{h_0^2} \equiv \gamma_2 \frac{u^2}{2}, \quad (15)$$

which defines the global confining potential,

$$\gamma_{0_2} \equiv \frac{KA}{h_0^2}. \quad (16)$$

Using the experimental values  $KA_2 \sim 2 \times 10^3 k_B T / \mu m^2$  and  $\gamma_{0_2} \sim 24 \times 10^3 k_B T / \mu m^4$  we have  $h_0 \sim 0.3 \mu m$ . Observing the height profiles of figure 2(C) it can be seen that  $h_0 \sim 0.4 \mu m$ , which is close to the estimated value above as well, supporting the global shape confinement proposed for the lower membrane. As mentioned before, the linear potential  $\gamma_2 = KA_2 \times 4(2\mathcal{H}_2^2 - K_2) + \gamma_{0_2}$  is a good approximation for points of the membrane far from the adhesion sites ( $\rho \leq 1$ ), where the membrane interacts weakly with the substrate. If this potential is subtracted from the total potential  $\gamma_2$ , a residual  $\gamma_R$  is obtained. It is suggested here that this residual potential is related to the substrate presence and thus maximum in the region of membrane adhesion. Indeed, the plot of  $\gamma_R$  versus the distance of the lower membrane to the substrate ( $h_2$ )(plot not shown) is approximately linear and has a maximum value at  $h_2 = 0$  (where the membrane touches the glass coverslip) and is null when  $h_2$  achieves its maximum value. Despite that, there are still many questions regarding this extra potential and more experiments are necessary for the proposal of a model.

### 3.5. Bending modulus $k_c$

The results for the bending modulus are presented in figure 5 (A) and (B), for upper and lower membranes, respectively. The empty symbols represent the data before correction for lateral movement and the full ones represent the data after correction. The grey area is the standard deviation of the mean value obtained with the ten final runs of the AG. According to *Gov et al.* [31]  $k_c$  is assumed approximately constant along the cell radius. The same is done by *Park et al.*, who uses in his spherical shell model [18] an unique value of  $k_c$  for the whole cell. Surprisingly, our data suggests that  $k_{c1}$  and  $k_{c2}$  vary throughout the cell membranes within the limits of  $[5 - 30] k_B T$ . The bending modulus  $k_{c1}$  for example has a value of  $\sim 6 k_B T$  in the middle of the cell and increases until it achieves a value of  $\sim 25 k_B T$  for  $\rho \sim 2 \mu m$ . This range comprises the different values of  $k_c$  measured for the whole cell using others techniques [18, 25]. Moreover, the

observed increase of  $k_{c1}$  with the cell radius might be the explanation why techniques that measure membrane fluctuations at the cell edge observe higher values for  $k_c$  than others that average the fluctuations over the cell area [18, 25].

A possible explanation to  $k_c$  alteration is that the RBC membranes thickness vary with position, since  $KA_1$  and  $KA_2$  remain practically constant along the cell. A relation between  $k_c$  and the thickness  $d$  of the membrane is given by [30],

$$k_c = \frac{KA d^2}{\alpha}, \quad (17)$$

where  $\alpha$  depends on the membrane geometry. We propose that each RBC membrane is composed by two thin elastic sheets (lipid bilayer and cytoskeleton) locally separated by a distance  $d$  (due to specific proteins) that can slowly vary along the cell radius, with compressibility modulus  $KA_m$  for the lipid bilayer and  $KA_c$  for the cytoskeleton. Following *Evans et al.* [32] we have that,

$$k_c = KA_{eff} d^2, \quad (18)$$

where  $KA_{eff}$  is an effective compressibility modulus given by,

$$KA_{eff} = \frac{KA_m KA_c}{KA_m + KA_c}. \quad (19)$$

Using as  $KA_{eff}$  the values  $KA_1$  and  $KA_2$  previously determined we obtain the thickness  $d_1$  and  $d_2$  of the upper and lower membranes, respectively, as shown in figure 5(C). The dots represent the upper membrane thickness ( $d_1$ ) and the squares represent the lower membrane thickness ( $d_2$ ). The thickness values correspond to the bilayer+cytoskeleton width and are within the range of (0.050 – 0.125)  $\mu\text{m}$ . Notably, those values are in agreement with compression experiments performed using a biomembrane force probe and optical interferometry [33]. Analyzing the upper membrane thickness profile it can be seen that  $d_1$  significantly increases for radius positions beyond 1.50  $\mu\text{m}$ , a behavior which was theoretically predicted by *Y. Fung and P. Tong* [34]. Additionally, the lower membrane thickness profile indicates that the membranes have approximately the same thickness value in the center of the cell, and decreases as the membrane gets closer to the substrate. The interaction membrane/glass substrate may be inducing a compression on the lower membrane.

### 3.6. Surface tension $\sigma$

In figure 6(A) and (B) the results for the surface tension  $\sigma_1$  and  $\sigma_2$  are presented, respectively. The empty symbols represent the data before correction for lateral movement and the full ones represent the data after correction. The grey area is the standard deviation of the mean value obtained with the ten final runs of the AG. The range of values [20 – 80]  $\mu\text{N}/\text{m}$  (considering  $T$  as the bath temperature), is at least tenfold higher than the ones reported by others authors [15, 25]. One possible explanation for that discrepancy is that the values are a measure of a mechanical tension and not a surface tension, as originally proposed by *Gov et al.* [31]. According to *Farago*

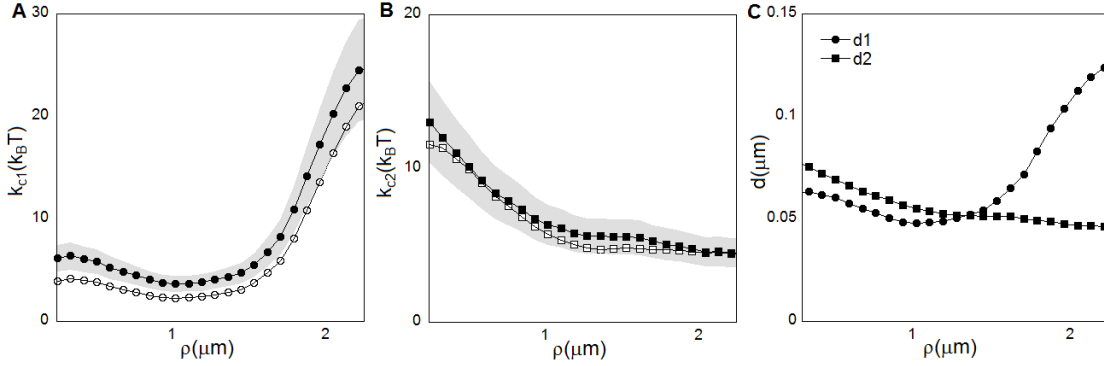


**Figure 5.** Bending modulus for each cell membrane: (A)  $k_{c1}$  and (B)  $k_{c2}$ . The unfilled symbols represent the non-corrected data and the filled symbols represent the corrected ones. The grey area is the standard deviation of the mean value obtained with the ten final runs of the AG. (C) Thickness profiles of the cell membranes (bilayer+cytoskeleton). The values are within the range of  $(0.050 - 0.125) \mu m$ , in accordance with compression experiments [33].

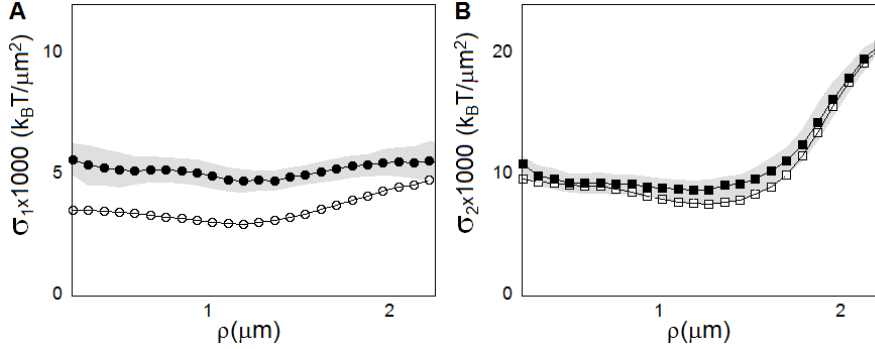


**Figure 6.** Surface tension for each cell membrane: (A)  $\sigma_1$  and (B)  $\sigma_2$ . The unfilled symbols represent the non-corrected data and the filled symbols represent the corrected ones. The grey area is the standard deviation of the mean value obtained with the ten final runs of the AG.

[35], the physical meaning of the term  $\sigma$  in the spectrum of equation 1 is actually a mechanical tension. *Farago* [35] defines the term  $\sigma$  as the lateral force per unit length exerted on the boundaries of a membrane when one attaches it to a frame. This idea is illustrated in figure 4(E), for the case of a red cell, where the membrane area adhered to the substrate is delimited by a circumference of radius  $R \cong 2 \mu m$ . If this is the case, the mechanical tension can be estimated as the adhesion force  $F_a$  by which the membrane is being pulled by the substrate, divided by the circumference length of the adhered region,

$$\sigma \sim \frac{F_a}{2\pi R}. \quad (20)$$

Considering  $\sigma_1 = 7 \times 10^3 k_B T / \mu m^2 \equiv 28 \mu N/m$  (with  $T$  the bath temperature), the adhesion force obtained for the upper membrane is  $\sim 350$  pN. For  $\sigma_2$ , the estimated force is approximately  $F_a \sim 500$  pN. Micropipette measurements [36] of the adhesion

force of red cells to common glass (hydrophilic) are between 500 to 1600 pN.

#### 4. Conclusions

In this paper the formulation of Defocusing Microscopy (DM) is exposed, together with its application to RBCs. Using the presented methods we can obtain total 3D total images of RBCs, volume, tridimensional thickness profile and determine the height profiles of each cell surface-membranes (bilayer+cytoskeleton), the upper one free to fluctuate and the lower one adhered to the substrate. Furthermore, by measuring DM contrast fluctuation and assuming a plane membrane model, the membrane height fluctuations along the cell radius of each surface-membrane can be extracted, separately, an unique feature of DM. The radial behavior of the elastic moduli of each surface-membranes are also obtained, allowing the discussion of physical aspects of the cell membrane. Finally, the methods presented here allow the extraction of biomechanical characteristics of red blood cells and thus can be used as tools to study several pathologies related to RBCs alteration.

#### 5. Acknowledgments

##### Acknowledgments

The authors acknowledge the support from the Brazilian agencies FAPEMIG, CAPES, CNPq, PRONEX-FACEPE, INFCx and declare no conflicts of interest. The authors also acknowledge B E de Faria and L Cescato for their help with the gratings experiments.

#### Appendix

##### *Appendix A: Defocusing microscopy*

A monochromatic light electric field  $E(\vec{r})$  with propagation direction along the  $z$  axis is considered for propagation. Fourier Optics [37] is used, in a way that,

$$E(\vec{\rho}) = \frac{1}{(2\pi)^2} \int A(\vec{q}) e^{i\vec{q}\cdot\vec{\rho}} d\vec{q}. \quad (\text{A.1})$$

with its inverse transform representing the angular spectrum  $A(\vec{q}, z)$  of the electric field,

$$A(\vec{q}) = \int E(\vec{\rho}) e^{-i\vec{q}\cdot\vec{\rho}} \vec{\rho}. \quad (\text{A.2})$$

The angular spectrum  $A$  is propagated through the phase object, lenses and free regions [2]. Using the paraxial approximation, the calculation returns the final electric field at image plane IP,

$$E(\vec{\rho}, z_f) = B e^{i\alpha(\vec{\rho})} (2\pi)^2 \int A_0(\vec{q}) e^{i\frac{z_f}{2k}q^2} e^{i\vec{q}\cdot\vec{\rho}} d\vec{q}, \quad (\text{A.3})$$



where  $B$  is a constant,  $\alpha(\vec{\rho})$  is a phase factor and  $A_0(\vec{q})$  is the angular spectrum immediately after crossing the specimen ( $z = 0$ ),  $k = n_{ob}k_0$ , with  $n_{ob}$  the objective immersion medium refractive index and  $k_0$  the vacuum light wavenumber. As it can be seen, a bright-field defocused microscope is similar to a phase-contrast microscope, but with a phase difference between the diffracted and nondiffracted light of  $\Delta\phi = \frac{z_f q^2}{2k}$ .

Considering the phase object as a specimen composed of a single thin interface with height profile  $h(\vec{\rho})$  and refractive index  $n + \Delta n$ , immersed in a medium of refractive index  $n$ , when an incident plane wave with field  $E_0$  crosses the object, it is diffracted [21] such that,

$$E(\vec{\rho}) = E_0 e^{i\Delta\varphi(\vec{\rho})} = E_0 e^{-i\Delta n k_0 h(\vec{\rho})}. \quad (\text{A.4})$$

In the limit of  $\Delta\varphi(\vec{\rho}) \ll 1$ ,  $E_0(\vec{\rho}, z) \simeq E_0[1 + i\varphi(\vec{\rho})] = E[1 - i\Delta n k_0 h(\vec{\rho})]$  and using the Fourier decomposition for the height profile  $h(\vec{\rho}) = \frac{1}{\sqrt{S}} \sum_{\vec{q}} h(\vec{q}) \sin(\vec{q} \cdot \vec{\rho})$ ,

$$E(\vec{\rho}) = E \left[ 1 - \frac{i\Delta n k_0}{\sqrt{S}} \sum_{\vec{q}} h(\vec{q}) \sin(\vec{q} \cdot \vec{\rho}) \right]. \quad (\text{A.5})$$

Substituting it into equation A.1,

$$A_0(\vec{q}) = (2\pi)^2 E_0 \left[ \delta(\vec{q}) + \frac{\Delta n k_0}{2\sqrt{S}} \sum_{\vec{q}'} h(\vec{q}') \delta(\vec{q} + \vec{q}') - \frac{\Delta n k_0}{2\sqrt{S}} \sum_{\vec{q}'} h(\vec{q}') \delta(\vec{q} - \vec{q}') \right], \quad (\text{A.6})$$

which is the angular spectrum after the object. Using this  $A_0$  in equation A.3 and defining the image contrast as  $C(\vec{\rho}) = \frac{I(\vec{\rho}) - I_0}{I_0}$ , where  $I(\vec{\rho})$  is the intensity of the object image and  $I_0$  is the background intensity, for first-order diffraction, the DM contrast is given by,

$$C(\vec{\rho}) = -\frac{2\Delta n k_0}{\sqrt{S}} \sum_{\vec{q}} \left[ h(\vec{q}) \sin(\vec{q} \cdot \vec{\rho}) \sin\left(\frac{z_f}{2k} q^2\right) \right]. \quad (\text{A.7})$$

For red blood cells the light electric field passes through both surface-membranes as in the model of figure 1(B). By assuming weakly diffracting objects, the incident light is diffracted by one or the other surface, with a negligible contribution due to diffraction by both surfaces. In this case the defocused electric field can be written as [2, 3, 4, 5, 6],

$$E(\vec{\rho}, z_f) = \frac{1}{(2\pi)^2} \int [A_1(\vec{q}) e^{i\vec{q} \cdot \vec{\rho}} e^{i\left(\frac{z_f - h_1(\vec{\rho})}{2k} q^2\right)} + A_2(\vec{q}) e^{i\vec{q} \cdot \vec{\rho}} e^{i\left(\frac{z_f - h_2(\vec{\rho})}{2k} q^2\right)}] d\vec{q} - E_0 \quad (\text{A.8})$$

where  $h_1(\vec{\rho})$ ,  $h_2(\vec{\rho})$  are the height profiles for upper and lower RBC surface-membranes (bilayer+cytoskeleton), respectively, and the terms,

$$\begin{aligned} A_1(\vec{q}) &= \int E_0 e^{-i\vec{q} \cdot \vec{\rho}} e^{i\Delta n k_0 h_1(\vec{\rho})} d\vec{\rho} \\ A_2(\vec{q}) &= \int E_0 e^{-i\vec{q} \cdot \vec{\rho}} e^{-i\Delta n k_0 h_2(\vec{\rho})} d\vec{\rho} \end{aligned} \quad (\text{A.9})$$

are the Angular Spectra of the electric field diffracted by the membranes. Additionally,  $\Delta n$  is the refractive index difference between the RBC and its surrounding medium. Considering equations A.8 and A.9, for first-order diffraction the DM contrast for a red cell is,

$$C(\vec{\rho}) = \frac{2\Delta n k_0}{\sqrt{S}} \left\{ \sum_{\vec{q}} \left[ h_2(\vec{q}) \sin\left(\frac{(z_f - h_2(\vec{\rho}))q^2}{2k}\right) - h_1(\vec{q}) \sin\left(\frac{(z_f - h_1(\vec{\rho}))q^2}{2k}\right) \right] \sin(\vec{q} \cdot \vec{\rho}) \right\}, \quad (\text{A.10})$$

where  $S$  is the RBC surface area.

### Appendix B: DM control experiments

In order to test the validity of the expressions above for DM, control experiments were performed using phase gratings with known amplitudes. The gratings height profiles were determined using Atomic Force Microscopy (AFM). The grating DM contrast measurements were conducted with a 100X oil immersion objective and using red filtered light of  $\lambda = (0.660 \pm 0.010) \mu\text{m}$ . The images were captured with a CCD camera at 15fps and the defocusing distance was controlled by a piezoelectric nanoposition stage. For details see Materials and methods section.

If a phase object with periodic structure is visualized through a defocused microscope its image contrast is repeatedly seen for a range of defocus distances. For a sinusoidal phase grating with height  $h(x) = h \sin(q_g x)$ , where the grating's wavenumber is  $q_g = \frac{2\pi}{\Lambda}$  and  $\Lambda$  is the groove spacing, using equation A.7 (since  $z \gg h$ ) the contrast (first order diffraction) along the  $x$  axis is given by,

$$C(x, z_f) = 2\Delta n k_0 h \sin(q_g x) \sin\left(\frac{z_f q_g^2}{2n_{ob} k_0}\right), \quad (\text{A.11})$$

where  $k_0$  is the incident wavenumber,  $n_{ob}$  is the objective immersion medium refractive index and  $\Delta n$  is the refractive index difference between the grating and its surrounding medium. The contrast as shown in equation A.11 is a combination of two sine terms, so that when the  $z$  axis is scanned the grating self-image fades and reappears until the incident light coherence is lost.

From the maximum amplitude of a grating contrast ( $C_{max} = (2\Delta n k_0 h)$ ), obtained when  $\frac{z_f q_g^2}{2n_{ob} k_0} = \frac{\pi}{2}$ , the grating's height  $h$  can be determined if  $\Delta n$  is known. Also, from the contrast periodicity in the  $x$  axis, given by  $\sin(q_g x)$ , the grating's groove spacing can be found, since  $q_g = \frac{2\pi}{\Lambda}$ . Finally, from the contrast periodicity in the  $z$  axis, given by  $\sin\left(\frac{z_f q_g^2}{2n_{ob} k_0}\right)$ , it can be confirmed that the appropriate light wavenumber to be used in the defocusing contrast term is  $k = k_0 n_{ob}$ . Here we use both the square contrast and contrast correlation in  $x$  to obtain the grating's parameters, since it provides a more accurate determination of the parameters involved due to a better averaging along the grating. The results are then compared with the ones measured using different techniques.

An image of a phase grating contrast at its maximum amplitude position is shown in figure A1(A). In (B) the correlation contrast  $\langle C(x')C(x'+x) \rangle$  along a horizontal line ( $x$  axis) of (A) is presented. The contrast correlation in  $x$  is given by,

$$\langle C(x')C(x'+x) \rangle = (\sqrt{2}\Delta nk_0h)^2 \cos(q_g x), \quad (\text{A.12})$$

which can be fitted to the data of plot (B), letting  $(\sqrt{2}\Delta nk_0h)^2$  and  $\Lambda$  as free parameters. The value for  $\Lambda$  with the error bar as returned by the fit is  $\Lambda = (1.3219 \pm 0.0001) \mu\text{m}$ , which is in agreement with AFM measurement  $\Lambda_{AFM} = (1.33 \pm 0.05) \mu\text{m}$ .

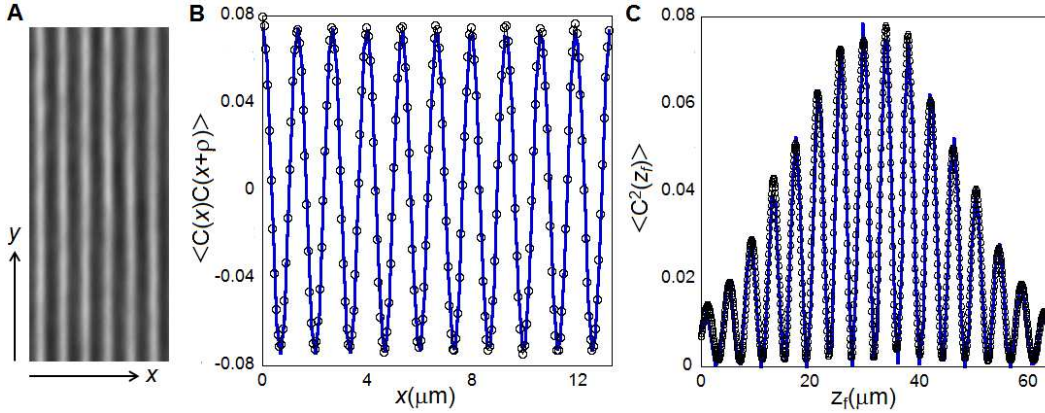


**Figure A1.** (A) Image of a phase grating contrast at its maximum amplitude position. (B) Correlation of contrast  $\langle C(x)C(x+\rho) \rangle$  along a horizontal line ( $x$  axis). (C) Average square contrast  $\langle C^2(z_f) \rangle$  along the  $z$  axis. The grating contrast along  $z_f$  varies periodically with a periodicity of  $\lambda_{DM}$ .

To determine the grating's height it is necessary to know the grating's refractive index, which can also be obtained experimentally using DM contrast measurements. When the grating is immersed in air, the maximum contrast observed for the grating is  $C_{air} = 2(n_g - n_{air})k_0h$ . However, if the grating is immersed in a different medium, with refractive index  $n_m$ , then the maximum contrast becomes  $C_m = 2(n_g - n_m)k_0h$ , such that,

$$\frac{C_{air}}{C_m} = \frac{n_g - n_{air}}{n_g - n_m} \quad \text{and thus,} \quad n_g = \frac{C_{air}n_m - C_m}{C_{air} - C_m}. \quad (\text{A.13})$$

In order to determine the grating refractive index we have covered it with an oil of known refractive index ( $n_{oil} = 1.51 \pm 0.01$ ). In that configuration we obtained a maximum contrast of  $C_m = 0.063$ . In air, the maximum contrast for the same grating was  $C_{air} = 0.31$ , such that the refractive index for the analyzed grating was found to be  $n_g = 1.64 \pm 0.02$ . This value is 4% higher than the one measured using the prism coupler technique.

In figure A1 (C) the average square contrast  $\langle C^2(z_f) \rangle = \frac{1}{A} \iint C^2(x, z_f) dx dy$  as a function of  $z_f$  axis is presented since this is an average over the entire image and provides better statistics. The plot was obtained by using the Histogram tool of Image J (Rasband WS. ImageJ, U.S. National Institutes of Health, Bethesda, Maryland, USA,

imagej.nih.gov/ij/, 19972012) [26] for the entire image of each frame, where the standard deviation divided by the mean intensity is equal to  $\sqrt{\langle C^2(z_f) \rangle}$ . By squaring it we obtain  $\langle C^2(z_f) \rangle$ . The envelope function of the incident light can be approximated by a gaussian function  $e^{-\frac{(\lambda-\lambda_0)^2}{2\Delta\lambda^2}}$ , where  $\lambda_0 = 0.660 \mu\text{m}$  and  $\Delta\lambda = 0.010 \mu\text{m}$  is the filter width, such that,

$$\langle C^2(z_f) \rangle = (\sqrt{2}\Delta n h k_0)^2 \sin^2 \left( \frac{(z_f - z_0)^2 q_g}{2n_{ob}k_0} \right) e^{-\frac{(z_f - z_0)^2}{2\xi_z^2}}, \quad (\text{A.14})$$

where  $\xi_z = \frac{\Lambda^2 n_{ob}}{2\pi\Delta\lambda}$  is the axial coherence length in this case. The function  $\langle C^2(z_f) \rangle$  varies periodically as a function of the distance  $z_f$  with the DM wavelength  $\lambda_{DM}$ ,

$$\frac{2\pi}{\lambda_{DM}} = \frac{q_g^2}{2n_{ob}k_0} = \frac{2\pi\lambda_0}{2\Lambda^2 n_{ob}}, \quad (\text{A.15})$$

such that  $\lambda_{DM} = n_{ob} \frac{2\Lambda^2}{\lambda_0}$ , which can be related to the Talbot length  $\lambda_T = \frac{2\Lambda^2}{\lambda_0}$  [38], then

$$\lambda_{DM} = n_{ob}\lambda_T. \quad (\text{A.16})$$

Equation A.14 was used to fit the data of  $\langle C^2(z_f) \rangle$ , leaving the terms  $(\sqrt{2}\Delta n h k_0)^2$ ,  $\lambda_{DM}$  and  $\xi_z$  and  $z_0$  as free parameters. The best fit is presented in figure A1(C) as the blue line and returned the values  $0.0793 \pm 0.0003$ ,  $(8.274 \pm 0.0002) \mu\text{m}$ ,  $(16.02 \pm 0.07) \mu\text{m}$  and  $(31.683 \pm 0.003) \mu\text{m}$ , respectively. Using the value for  $(\sqrt{2}\Delta n h k_0)^2$ ,  $\lambda_0 = 0.660 \mu\text{m}$  and  $\Delta n = 0.064$  (determined previously) we get the grating's height  $h = 0.033 \pm 0.001 \mu\text{m}$ , which compares well with the value  $h_{AFM} = 0.0361 \pm 0.0002 \mu\text{m}$  returned by AFM measurements. From the fit we also find that  $\lambda_{DM} = (8.274 \pm 0.002) \mu\text{m}$  together with the Talbot length  $\lambda_T = (5.30 \pm 0.08) \mu\text{m}$ , which results from equation A.16 the value  $n_{ob} = 1.56 \pm 0.02$ , slightly higher than the manufacturer's value of 1.51. This confirms that  $k = n_{ob}k_0$ , as predicted by our model of defocusing, as the proper wavenumber  $k$  to be used. In the case of a dry objective the correct wavenumber is  $k = k_0$ . Additionally, if the recording video-camera is the element displaced to cause image defocusing, then the phase shift is scaled by other parameters and one can relate the displacement of the video-camera to the displacement of the objective to produce the same amount of defocusing. In this case, it is obtained that  $z_{camera} = M^2 z_{objective}$ , where M is the magnification of the objective. Finally, the value for  $\xi_z = (16.02 \pm 0.07) \mu\text{m}$  gives the axial coherence length. From the expression for  $\xi_z$  we obtain that  $\Delta\lambda \sim 0.027 \mu\text{m}$ , larger than the filter width  $\Delta\lambda = 0.010 \mu\text{m}$ , which suggests that additional effects are occurring.

### Appendix C: Genetic Algorithm

A GA is a search algorithm based on the mechanisms of Darwinian evolution that uses random mutation, crossover, and selection operators to breed better solutions from an originally random starting population [39]. GAs have been widely used to solve complex problems in different areas of knowledge like engineering, management and medicine. In this paper a GA was implemented and employed to obtain the power spectrums

$\langle |u_1(\vec{q})|^2 \rangle$  and  $\langle |u_2(\vec{q})|^2 \rangle$  using equation 1 as fitting equation. Preliminary tests with five of the major benchmarking functions for GA testing presented in [40] were used to evaluate its performance. The five selected functions have known global optimal and different degrees of complexity: F1 is smooth unimodal and strongly convex, F2 has a very narrow ridge with sharp tips, F5 has many local optima, F7 has a wide search space and a large number of local minima and F8 is nonlinear and multimodal. GAs have difficulties to converge close to the minimum of such functions, because due to their characteristics, the probability of making progress decreases rapidly as the global optimal is approached. The tests consisted in 100 executions for each function with 90000 function evaluation per execution. The GA converged in all tests achieving high repeatability with small standard deviation of the solutions, showing that it is capable of solving complex problems. The searches were started with a random population of  $x$  individuals 20 fold the number of variables of the fitting equation. For equation 4 each individual described an elastic parameter, such that the number of variables was 150 and an initial population of 3000 individuals was used. In this case, a search space was defined for each elastic parameter:  $k_c = [0, 100]k_B T$ ,  $\gamma = [0, 50000]k_B T/\mu\text{m}^4$  and  $\sigma = [0, 500000]k_B T/\mu\text{m}^2$  where  $k_B$  is the Boltzmann constant and  $T$  temperature in Kelvin ( $T = 299\text{ K}$  for the experiments). Those limits were continuously decreased as the algorithm zone of convergence was delimited. Giving a random starting population, the GA iteratively performs evolution operations to breed a new generation of individuals, until some stop criterion is satisfied [39]. More specifically, in each generation the individual's fitness is assessed by calculating  $\Psi^2$ , given by  $\Psi^2 = \sum_i^N (T_i - t_i)^2$ , where  $T$  is the target data set ( $\langle \Delta C^2(i) \rangle$ ),  $t$  is the individual's data set of the generation and  $N$  is the number of variables. Theoretically, the stop criteria should be that  $\Psi^2$  reaches the value of zero. However, since the target data set is an experimental measurement, the intrinsic uncertainties must be taken into account. Therefore, the final solution was found when consecutive fitness values returned by best individuals had not changed by more than 1% of the experimental data variance for 1000 generations, starting the count from fitness values below 10% of the experimental data variance. In order to qualitatively access the robustness of the algorithm to initial conditions, the GA was executed several times with random initial population. In each run an average of  $5 \times 10^6$  function evaluations were necessary for the algorithm to converge. In figure 3(A) the ten final fitting results for  $\langle \Delta C^2 \rangle$  over 42 RBC are presented. The AG takes approximately 10 hours to converge in computers with *i7* Intel Core (Intel Company, Santa Clara, CA) processors and 32G of RAM memory.

#### *Appendix D: Correction for cell lateral movement*

What is measured with DM is the membrane fluctuation along the  $z$  axis ( $u_z$ ). This fluctuation can be decomposed into a normal ( $u_N$ ) and a tangent ( $u_T$ ) components to the membrane surface, as in figure A2. Thus,  $u_z$  is the  $z$  projection of  $\vec{u}_{total} = \vec{u}_N + \vec{u}_T$  and since equation 1 is related to the fluctuation  $u_N$ ,  $u_N$  has to be extracted from

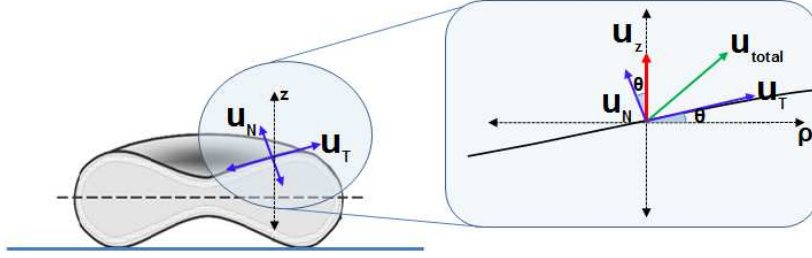


**Figure A2.** The two components of the cell total fluctuation  $u_{total}$ :  $u_T$  along the surface tangent and  $u_N$  along the normal to the surface. The  $z$  axis represents the axis along which the fluctuation is collected in DM technique ( $u_z$ ). To obtain  $u_N$  (height fluctuation) from  $u_z$ , a correction is needed.

the data of  $u_z$ . In figure A2,  $\theta$  is the angle formed between  $u_N$  and the  $z$  axis, then  $\langle (u_z)^2 \rangle = \langle (u_N)^2 \rangle \cos^2 \theta + \langle (u_T)^2 \rangle \sin^2 \theta$ , and is also the angle formed between  $u_T$  and the  $\rho$  axis, such that  $\tan \theta = \frac{dh}{d\rho}$ , where  $h$  is the membrane height profile. The value for  $u_z$  is equal  $u_N$  when  $\theta = 0$  (middle of the cell), where from figure 3 (B) we see that  $u_{z(rms)} \sim 10$  nm. Additionally,  $u_T$  may be assumed to be caused by the cell shear movement,  $\langle (u_T)^2 \rangle \simeq \frac{k_B T}{\mu} \simeq 5 \times 10^{-16} m^2$ , for a shear modulus  $8 \times 10^{-6} \mu N m^{-1}$  [18], resulting in a  $u_{T(rms)}$  value of 22 nm. Measuring the cell border fluctuations (where  $u_{N(rms)} \sim 0$ ) using DM, it is found that  $u_{T(rms)} \sim (16 - 22)$  nm, in agreement with the above estimation. Since at the cell center, where  $u_T \sim 0$ , the value  $u_{N(rms)} \sim 10$  nm is obtained, then  $u_{T(rms)} \simeq 2u_{N(rms)}$  and

$$\langle (u_N)^2 \rangle \simeq \frac{\langle (u_z)^2 \rangle}{4 - 3\cos^2 \theta}. \quad (\text{A.17})$$

## References

- [1] Diez-Silva M, Dao M, Han J, Lim C T and Suresh S 2010 Shape and biomechanical characteristics of human red blood cells in health and disease *MRS Bull* **35** 382
- [2] Agero U, Monken C H, Ropert C, Gazzinelli R T and Mesquita O N 2003 Cell Surface Fluctuations Studied with Defocusing Microscopy *Phys. Rev. E* **67** 051904
- [3] Neto J C, Agero U, Oliveira D C, Gazzinelli R T and Mesquita O N 2005 Real-time measurements of surface dynamics on macrophages and the phagocytosis of Leishmania parasites *Exp. Cell Res.* **303** 207-34
- [4] Neto J C, Agero U, Gazzinelli R T and Mesquita O N 2006 Measuring optical and mechanical properties of a living cell with Defocusing Microscopy. *Biophys. J.* **91** 1108-15
- [5] Mesquita L G, Agero U, and Mesquita O N 2006 Defocusing Microscopy: an approach for red blood cell optics *Appl. Phys. Lett.* **88** 133901
- [6] Glionna G, Oliveira C K, Siman L G, Moyses H W, Prado D M U, Monken C H and Mesquita O N 2009 Tomography of fluctuating biological interfaces using defocusing microscopy *Appl. Phys. Lett.* **94** 193701
- [7] Roma P M S, Siman L, Amaral F T, Agero U and Mesquita O N 2014 Total three-dimensional imaging of phase objects using defocusing microscopy: Application to red blood cells *Appl. Phys. Lett.* **104** 251107
- [8] Etcheverry S, Gallardo M J, Solano P, Suwalsky M, Mesquita O N and Saavedra C 2012 Real-time

- study of shape and thermal fluctuations in the echinocyte transformation of human erythrocytes using defocusing microscopy *J. Biomed. Opt.* **17** 106013
- [9] Suwalsky M, Belmar J, Villena F, Gallardo M J, Jemiola-Rzeminska M, Strzalka K 2013 Acetylsalicylic acid (aspirin) and salicylic acid interaction with the human erythrocyte membrane bilayer induce in vitro changes in the morphology of erythrocytes *Arch. of Biochem. and Biophys.* **539** 919
- [10] Zernike F 1942 Phase-contrast, a new method for microscopic observation of transparent objects, part I *Physica.* **9** 686-98
- [11] Nomarski G 1955 Nouveau dispositif pour l'observation en contraste de phase différentiel *J. Phys. Radium.* **16** 9-11
- [12] Gureyev T E and Nugent K A 1997 Rapid quantitative phase imaging using the transport intensity equation *Opt. Commun.* **133** 339-46
- [13] Paganin D and Nugent K A 1998 Noninterferometric phase imaging with partially coherent light *Phys. Rev. Lett.* **80** 2586-89
- [14] Barone-Nugent E D, Barty A and Nugent K A 2002 Quantitative phase-amplitude microscopy I: optical microscopy. *J. Microsc.* **206** 194-206
- [15] Popescu G, Park Y, Choia W, Dasaria R R, Feld M S, and Badizadegana K 2008 Imaging red blood cell dynamics by quantitative phase microscopy. *Blood Cells, Mol. Dis.* **41** 10-6
- [16] Kononenko V L 2011 Characterization of red blood cells rheological and physiological state using optical flicker spectroscopy *Advanced Optical Flow Cytometry: Methods and Disease Diagnoses* ed V. V. Tuchin (Weinheim: Wiley-VCH Verlag GmbH & Co. KGaA) pp 155-210
- [17] Park Y, Best C A, Auth T, Gov N, Safran S, Popescu G, Suresh S and Feld M S 2010 Metabolic remodeling of the human red blood cell membrane *Proc. Natl. Acad. of Sci.* **107** 1289-94
- [18] Park Y, Best C A, Badizadegana K, Dasari R R, Feld M S, Kuriabova T, Henle M L, Levine A J and Popescu G 2010 Measurement of red blood cell mechanics during morphological changes. *Proc. Natl. Acad. of Sci.* **107** 6731-36
- [19] Teague M R 1983 Deterministic phase retrieval: a Greens function solution. *J. Opt. Soc. Am.* **73** 1434-41
- [20] Kim T, Zhou R, Mir M, Babacan S D, Carney P S, Goddard L L and Popescu G 2014 White light diffraction tomography of unlabelled live cells *Nature Photon.* **8** 25663
- [21] Born M and Wolf E 1999 *Principles of Optics* (Cambridge: Cambridge University Press)
- [22] Brochard F and Lennon J F 1975 Frequency spectrum of the flicker phenomenon in erythrocytes *Le Journal de Physique* **11** 1035-47
- [23] Auth T, Safran S A and Gov N S 2007 Fluctuations of coupled fluid and solid membranes with application to red blood cells *Phy. Rev. E* **76** 051910
- [24] Levin S, and Korenstein R 1991 Membrane fluctuations in erythrocytes are linked to MgATP-dependent dynamic assembly of the membrane skeleton, *Biophys J.* **60** 733-37
- [25] Yoon Y, Hong H, Brown A, Kim D C, Kang D J, Lew V L and Cicuta P 2009 Flickering analysis of erythrocyte mechanical properties: dependence on oxygenation Level, cell Shape, and hydration Level *Biophys. J.* **97** 160615
- [26] Schneider C A, Rasband W S and Eliceiri K W 2012 NIH Image to ImageJ: 25 years of image analysis *Nat. Methods* **9** 671-75
- [27] Rappaz B, Barbul A, Emery Y, Korenstein R, Depeursinge C, Magistretti P J and Marquet P 2008 Comparative study of human erythrocytes by digital holographic microscopy, confocal microscopy and impedance volume analyzer *Cytometry A* **73** 895
- [28] Boss D, Hoffmann A, Rappaz B, Depeursinge C, Magistretti P J, Van de Ville D and Marquet P 2012 Spatially-resolved eigenmode decomposition of red blood cells membrane fluctuations questions the role of ATP in flickering *PLoS One* **8** 1-10
- [29] Safran S 1994 *Statistical thermodynamics of surfaces, interfaces, and membranes* (Massachusetts: Addison-Wesley Pub.)
- [30] Boal D 2002 *Mechanics of the Cell* (Cambridge: Cambridge University Press)

- [31] Gov, N., A. Zilman and S. Safran. 2003. Cytoskeleton confinement and tension of red blood cell Membranes. *Phys. Rev. Lett.* **90**:228101.
- [32] Evans E 1974 Bending resistance and chemically induced moments in membrane bilayers *Biophys. J.* **14** 923-31
- [33] Heinrich V, Ritchie K, Mohandas N and Evans E 2001 Elastic thickness compressibility of the red cell membrane. *Biophys. J.* **81** 1452-63
- [34] Fung Y and Tong P 1968 Theory of sphering of red blood cells *Biophys. J.* **18** 175-98
- [35] Farago O 2011 Mechanical surface tension governs membrane thermal fluctuations *Phys. Rev. E* **84** 051914
- [36] Francis G W, Fisher L R, Gamble R A and Gingell D 1987 Direct measurements of cell detachment force on single cells using a new electromechanical method *J. of Cell Sci.* **87** 519-23
- [37] Goodman J W 1996 *Introduction to Fourier Optics* (New York: McGraw-Hill Co. Inc.)
- [38] Rayleigh L 1881 On copying diffraction-gratings, and on some phenomena connected therewith *Phil. Mag.* **11** 196-205
- [39] Koza J R 1998 *Genetic programming* (Cambridge: The MIT Press)
- [40] Digalakis J G and Margaritis K G 2001 On benchmarking functions for genetic algorithms *International Journal of Computer Mathematics* **77** 481-506